Supplementary Information: Atlantic overturning inferred from air-sea heat fluxes indicates no decline since the 1960s

Jens Terhaar[1,4,5*], Linus Vogt[1,2], Nicholas P. Foukal[1,3]

[1] Woods Hole Oceanographic Institution, Woods Hole, MA, USA

[2] Laboratoire d'Océanographie et du Climat Expérimentations et Approches Numériques (LOCEAN), Sorbonne Université, CNRS/IRD/MNHN, Paris, France

[3] Skidaway Institute of Oceanography, University of Georgia, Savannah, GA, USA

[4] Current Address: Climate and Environmental Physics, Physics Institute, University of Bern, Bern, Switzerland

[5] Current Address: Oeschger Center for Climate Change Research, University of Bern, Switzerland

***Jens Terhaar (now at University of Bern, Switzerland)**

Woods Hole Oceanographic Institution

Department of Physical Oceanography

266 Woods Hole Road

Woods Hole, MA 02543-1050

United States of America

jterhaar@whoi.edu

Supplementary Table 1: CMIP6 models used in this study and the corresponding model groups.

Model name	Modelling centre	References
ACCESS-CM2	Commonwealth Scientific and Industrial Research Organisation (CSIRO)	Ziehn et al. (2020)[123]
ACCESS-ESM1-5		
CanESM5	Canadian Centre for Climate Modelling and Analysis	Swart et al. (2019)[124]
CanESM5-CanOE		Christian et al. (2022)[125]
CESM2	Community Earth System Model contributors	Danabasoglu et al. (2020)[126]
CESM2-WACCM		
CMCC-CM2-SR5	Centro euro-Mediterraneo sui Cambiamenti Climatici	Cherchi et al. (2019)[127]
CMCC-ESM2		Lovato et al. (2022)[128]
CNRM-CM6-1-HR	Centre national de recherches météorologiques (CNRM)	Voldoire et al. (2019)[129]
CNRM-CM6-1		
CNRM-CM6-ESM2-1		Séférian et al. (2019)[130]
GFDL-CM4	Geophysical Fluid Dynamics Laboratory	Held et al. (2019)[131]
GFDL-ESM4		Dunne et al. (2020)[132]
GISS-E2-1-G	NASA Goddard Institute for Space Studies	Kelley et al. (2020)[133]
HadGEM3-GC31-LL	Met Office Hadley Centre	Andrews et al. (2020)[134]
HadGEM3-GC31-MM		
UKESM1-0-LL		Sellar et al. (2020)[135]
IPSL-CM6A-LR	Institut Pierre Simon Laplace (IPSL)	Boucher et al. (2020)[136]
MIROC6	Japan Agency for Marine-Earth Science and Technology (JAMSTEC) and Centre for Climate System Research / National Institute for Environmental Studies, Japan	Tatebe et al. (2019)[137]
MPI-ESM1-2-HR	Max-Planck-Institute for Meteorology	Mauritsen et al. (2019)[138], Gutjahr et al. (2019)[139]
MPI-ESM1-2-LR		
MRI-ESM2-0	Meteorological Research Institute	Yukimato et al. (2019)[140]
NorESM2-LM	Norwegian Climate Centre	Seland et al. (2020)[141]
NorESM2-MM		Tjiputra et al. (2020)[142]

Supplementary Table 2: CMIP5 models used in this study and the corresponding model groups.

Model name	Modelling centre	References
ACCESS1-0 ACCESS1-3 CSIRO-Mk3-6-0	Commonwealth Scientific and Industrial Research Organisation (CSIRO)	Bi et al. (2013)[143], Collier et al. (2013)[144]
FGOALS-s2	State Key Laboratory of Numerical Modeling for Atmospheric Sciences and Geophysical Fluid Dynamics	Bao et al. (2013)[145]
MIROC5	Japan Agency for Marine-Earth Science and Technology (JAMSTEC) and Centre for Climate System Research / National Institute for Environmental Studies, Japan	Watanabe et al. (2010)[146]
MRI-CGCM3	Meteorological Research Institute	Yukimoto et al. (2012)[147]
NorESM1-ME NorESM1-M	Norwegian Climate Centre	Bentsen et al. (2013)[148], Iversen et al. (2013)[149]

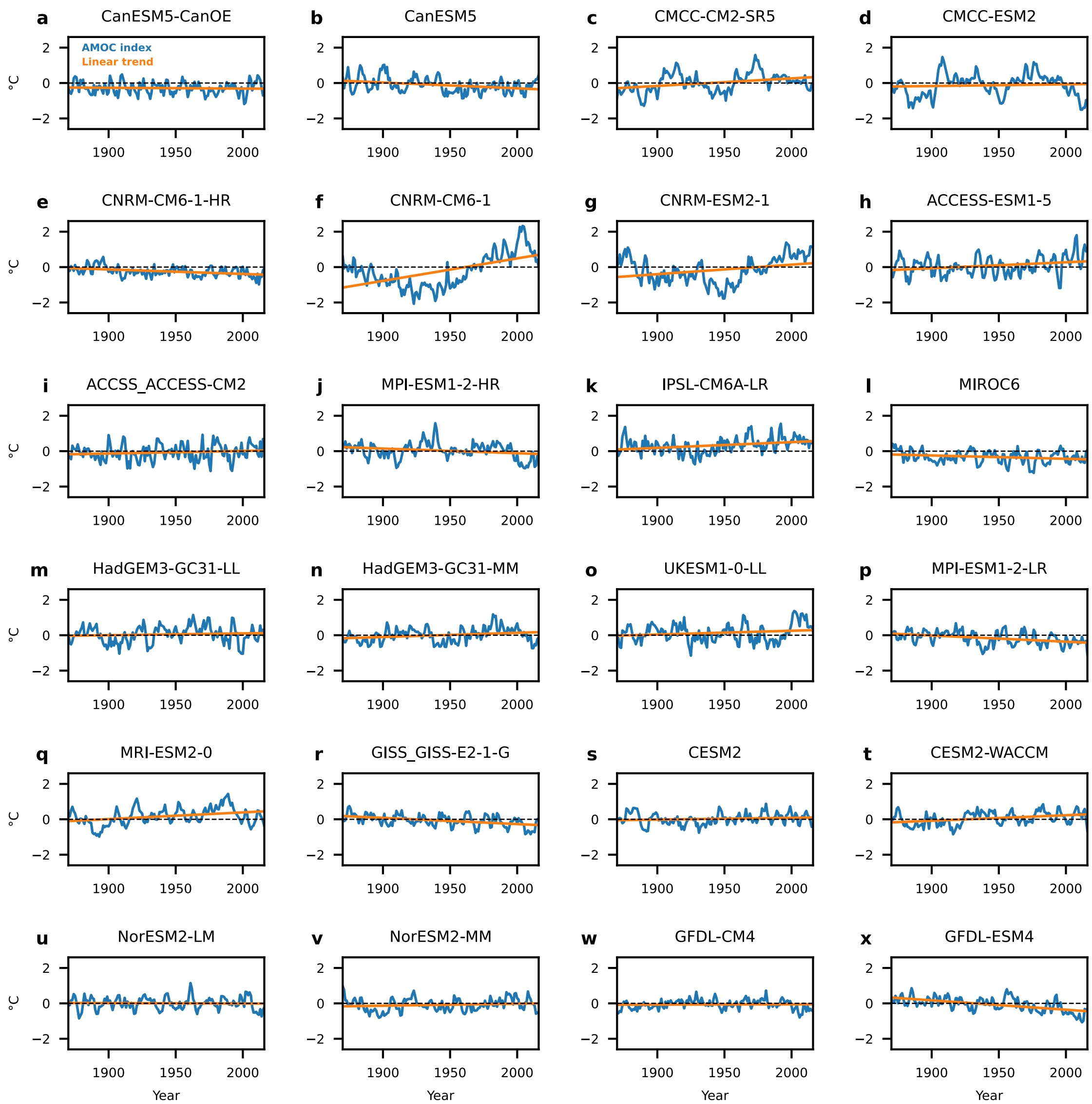

Supplementary Figure 1. Simulated SST-based AMOC index from 1870 to 2016 for 24 individual Earth System Models. The simulated AMOC index (blue lines) from 1870 to 2016 as defined by Caesar et al. (2018): North Atlantic SST anomalies with respect to global-mean SST averaged from November to May for 24 climate models from CMIP6. In addition, a linear fit (orange lines) is shown for each model. For each simulation, output is used from the historical simulations until 2014 and from SSP5-8.5 since 2015. SSP5-8.5 was chosen as all climate models provide output for that pathway and because differences in atmospheric CO_2 between the different SSPs from 2015 to 2020 are so small that these differences do not significantly impact the climate yet.

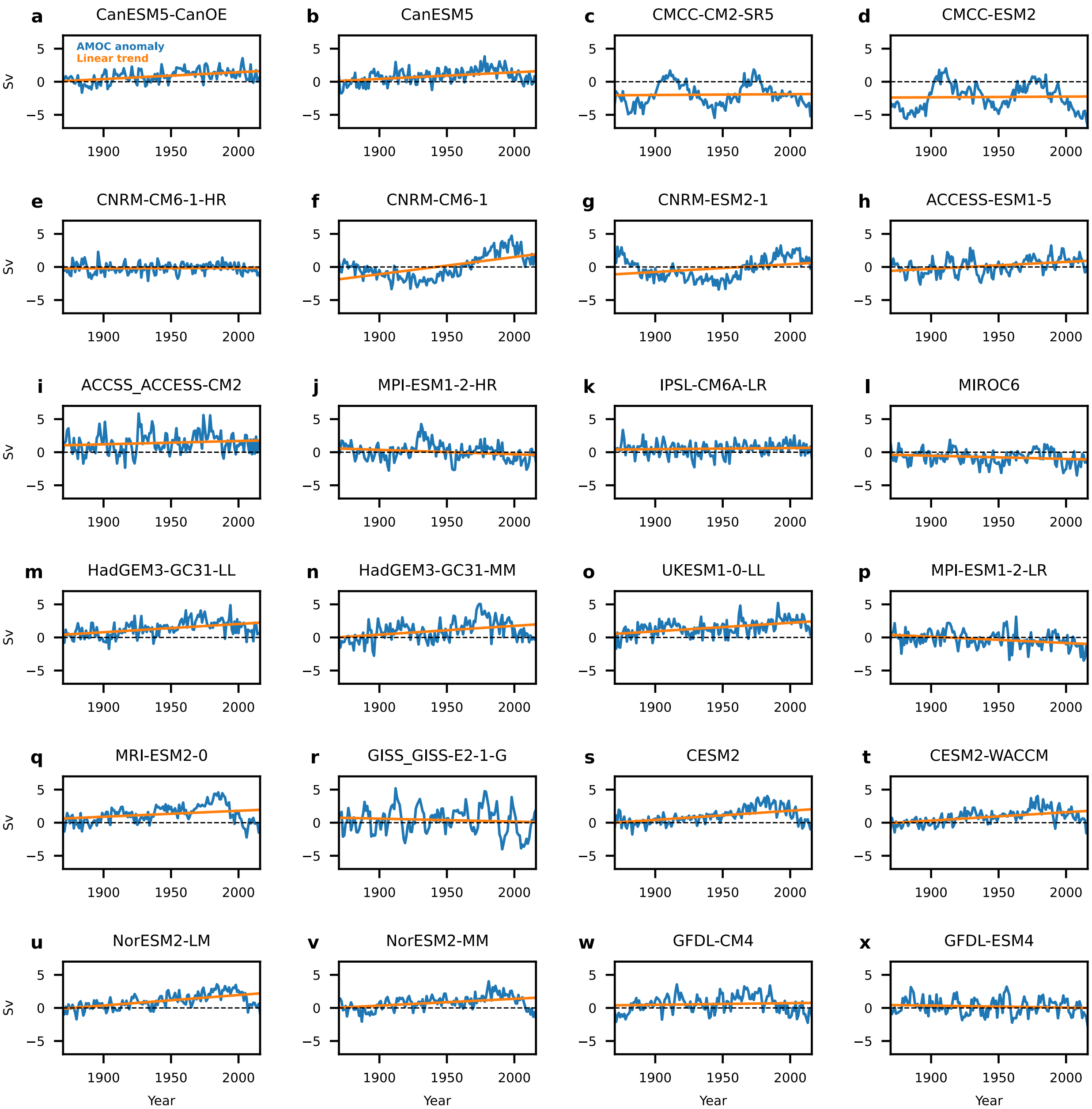

Supplementary Figure 2. Simulated AMOC anomaly from 1870 to 2016 for 24 individual Earth System Models. The simulated annually averaged AMOC anomaly (blue lines) for 24 Climate models from CMIP6 from 1870 to 2016. In addition, a linear fit (orange lines) is shown for each model. For each simulation, output is used from the historical simulations until 2014 and from SSP5-8.5 since 2015. SSP5-8.5 was chosen as all Climate models provide output for that pathway and because differences in atmospheric CO2 between the different SSPs from 2015 to 2020 are so small that these differences do not significantly impact the climate yet.

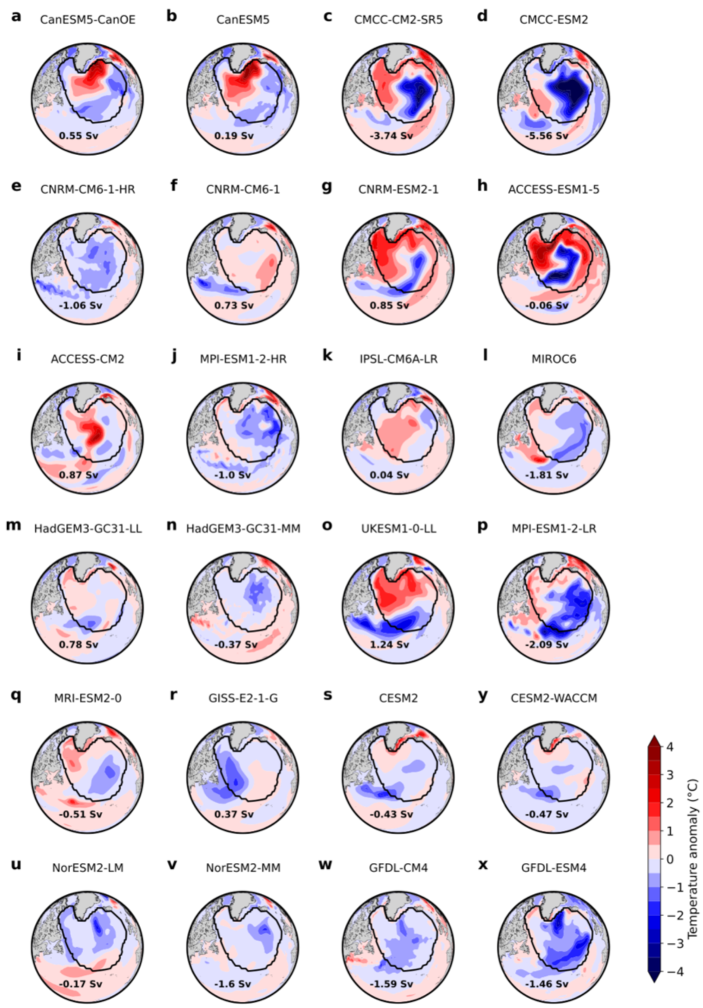

Supplementary Figure 3. Sea surface temperature and AMOC anomaly. North Atlantic sea surface temperature anomalies with respect to globally averaged sea surface temperatures averaged from November to May and from 2011 to 2020 for 24 climate models from CMIP6. The numbers at the bottom left of each map indicate the AMOC anomalies from 2011 to 2020 with respect to the pre-industrial AMOC for each model for the same decade. The black lines indicate the subpolar gyre as defined by Caesar et al. (2018). For each simulation, output is used from the historical simulations until 2014 and from SSP5-8.5 since 2015. SSP5-8.5 was chosen as all climate models provide output for that pathway and because differences in atmospheric CO_2 between the different SSPs from 2015 to 2020 are so small that these differences do not significantly impact the climate yet. The maps were produced using the Basemap tool in Python.

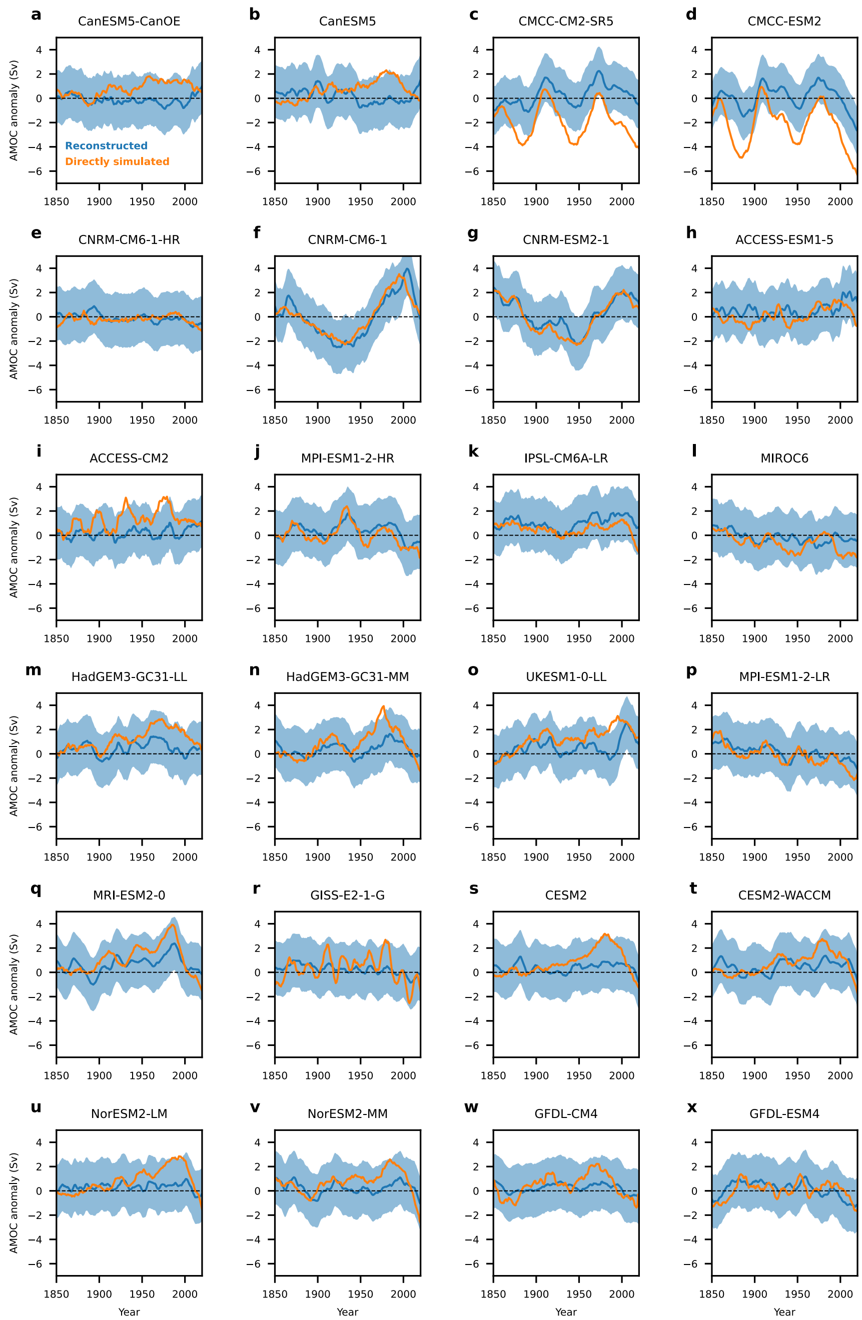

Supplementary Figure 4. Directly simulated and reconstructed decadal averaged AMOC anomalies at 26.5°N based on subpolar gyre sea surface temperature anomalies. The simulated decadal averaged AMOC anomaly at 26.5°N (orange line) and the reconstructed AMOC anomalies at 26.5°N based on the SPG SST index anomalies (blue line) for 24 climate models (**a-x**). The blue shading shows the 2-sigma standard deviation that results from uncertainty of the linear fit. The dashed black line shows zero anomalies.

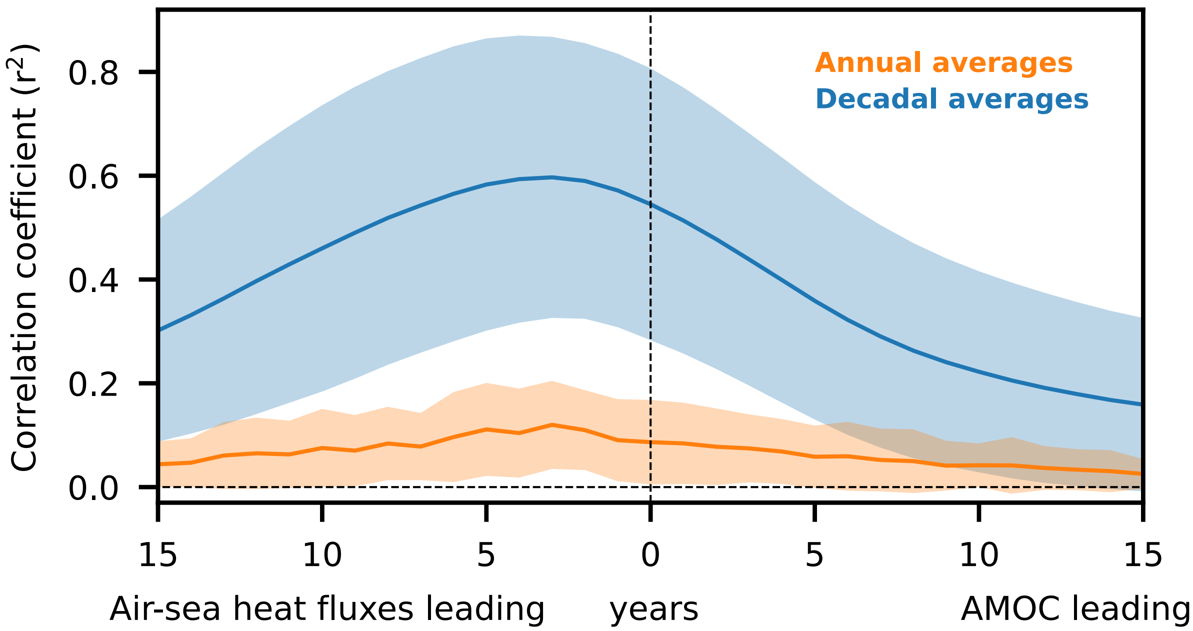

Supplementary Figure 5. Correlation between annual and decadal averaged AMOC and air-sea heat flux anomalies for a range of different leads and lags between both anomalies. Annual (orange) and decadal (blue) averaged AMOC and air-sea heat flux anomalies are calculated from 1850 to 2016. Correlations between both anomalies are calculated for differences in time between both anomalies of ±15 years. The lines indicate the average r^2 over 24 climate models for each lead-lag year and the shadings the standard deviation across all climate models.

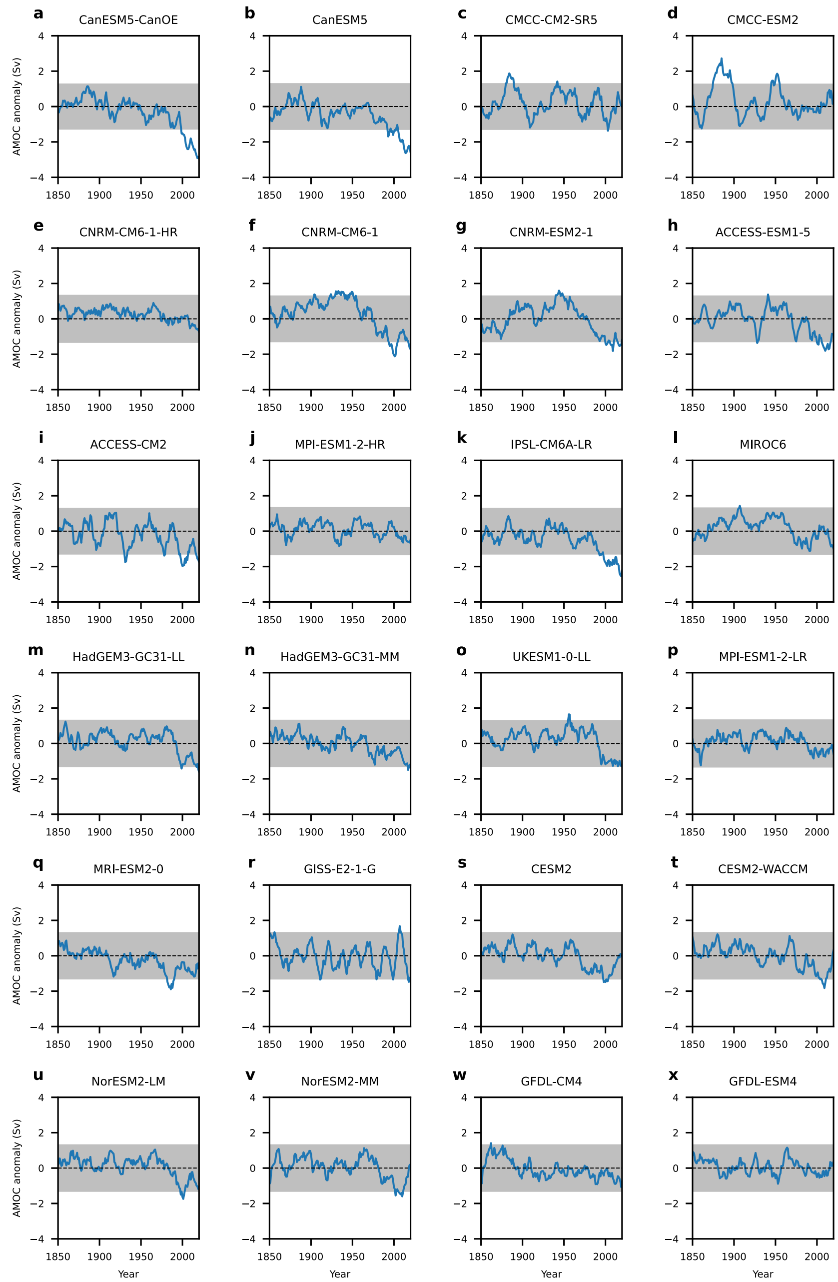

Supplementary Figure 6. Difference between directly simulated and reconstructed decadal averaged AMOC anomalies at 26.5°N in each climate model. The simulated decadal averaged AMOC anomaly at 26.5°N (orange line) and the reconstructed AMOC anomalies at 26.5°N based on air-sea heat flux anomalies (blue line) for 24 climate models from 1850 to 2020 (**a-x**). Negative values indicate that the reconstructed AMOC is smaller than the directly simulated AMOC. The grey shading shows the 2-s standard deviation that results from the uncertainty of the linear fit. The dashed black line shows zero anomalies.

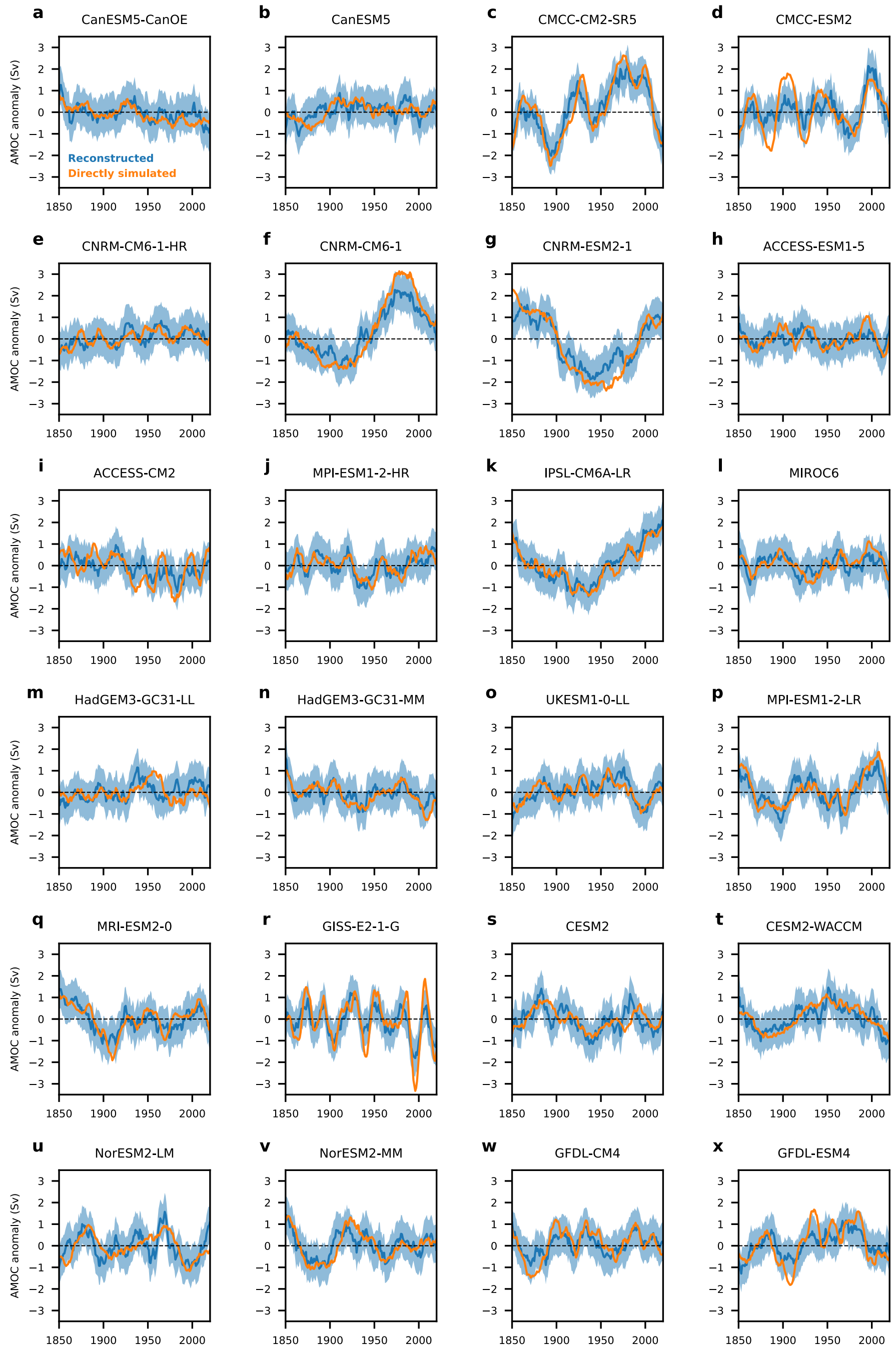

Supplementary Figure 7. Directly simulated and reconstructed decadal averaged AMOC anomalies at 26.5°N in each climate model for the pre-industrial control simulations. The simulated decadal averaged AMOC anomaly at 26.5°N (orange line) and the reconstructed AMOC anomalies at 26.5°N based on air-sea heat flux anomalies (blue line) for 24 climate models (**a-x**). The blue shading shows the 2-sigma standard deviation that results from uncertainty of the linear fit. The dashed black line shows zero anomalies.

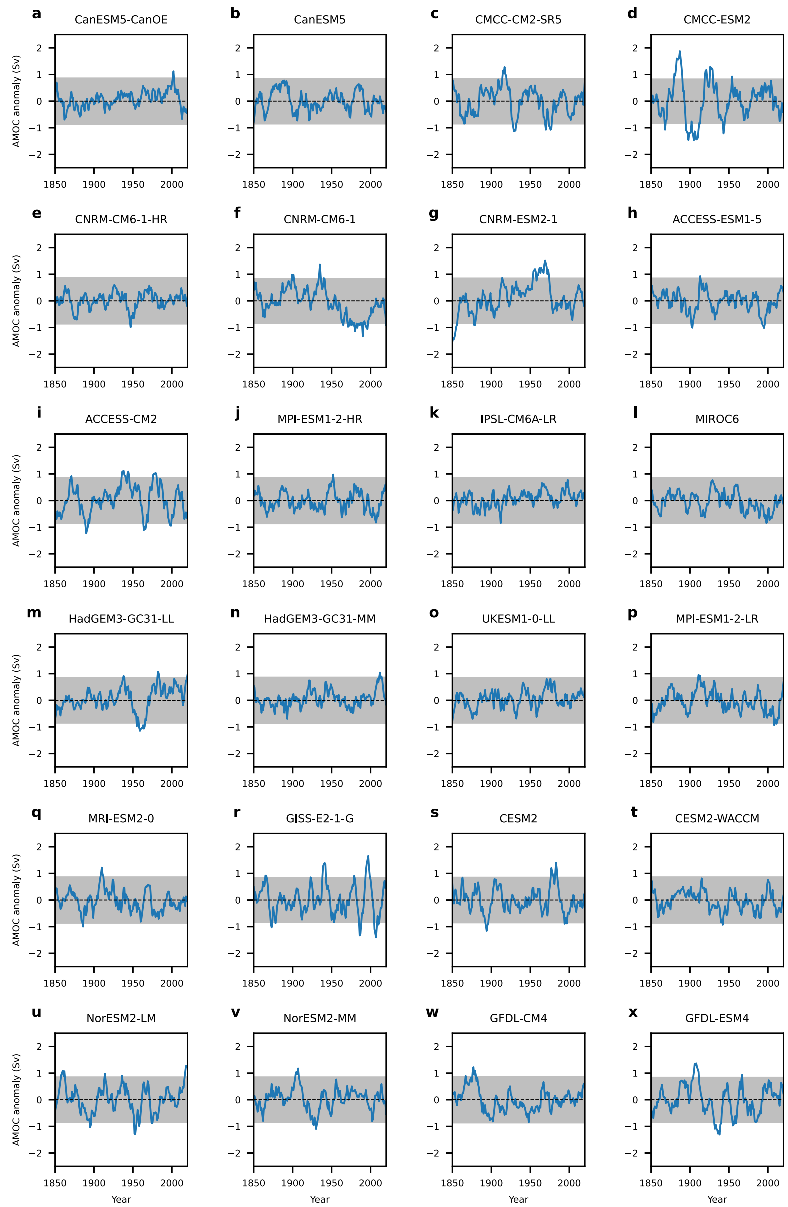

Supplementary Figure 8. Difference between directly simulated and reconstructed decadal averaged AMOC anomalies at 26.5°N in each climate model for the pre-industrial control simulation. The difference between the simulated decadal averaged AMOC anomaly at 26.5°N (orange line) and the reconstructed AMOC anomalies at 26.5°N based on air-sea heat flux anomalies (blue line) for 24 climate models from 1850 to 2020 in the pre-industrial control simulation (**a-x**). Negative values indicate that the reconstructed AMOC is smaller than the directly simulated AMOC. The grey shading shows the 2-s standard deviation that results from the uncertainty of the linear fit. The dashed black line shows zero anomalies.

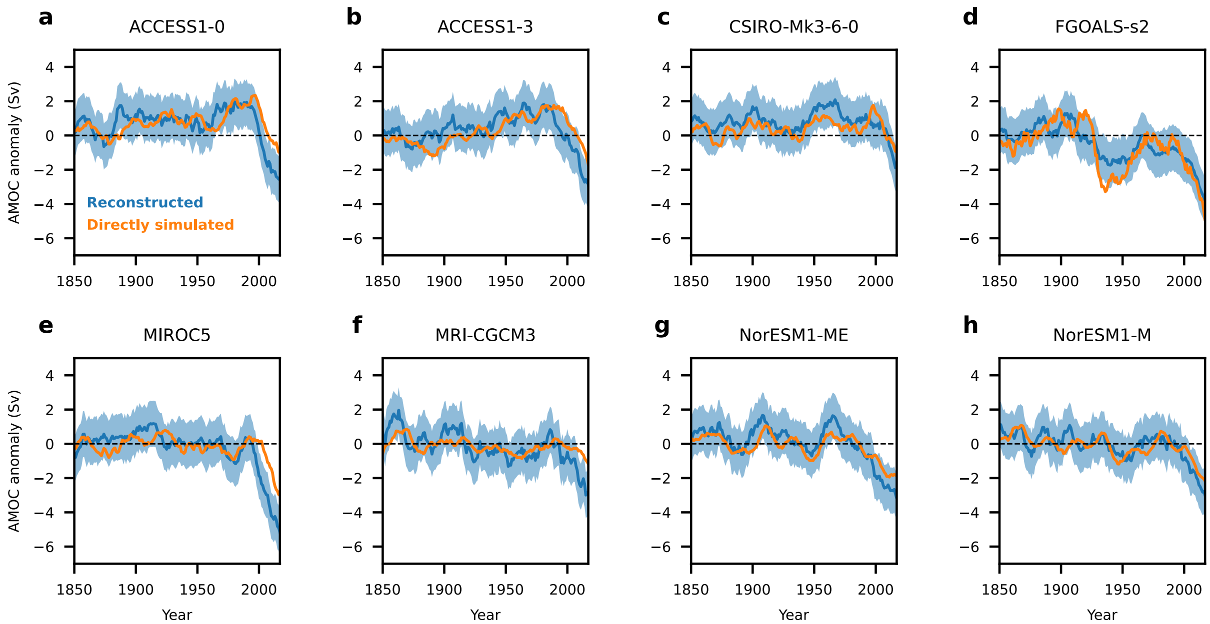

Supplementary Figure 9. Directly simulated and reconstructed decadal averaged AMOC anomalies at 26.5°N in each climate models from CMIP5. The simulated decadal averaged AMOC anomaly at 26.5°N (orange line) and the reconstructed AMOC anomalies at 26.5°N based on air-sea heat flux anomalies (blue line) for 8 climate models (**a-h**) from CMIP5 (Supplementary Table 2). The blue shading shows the 2-sigma standard deviation that results from uncertainty of the linear fit. The dashed black line shows zero anomalies.

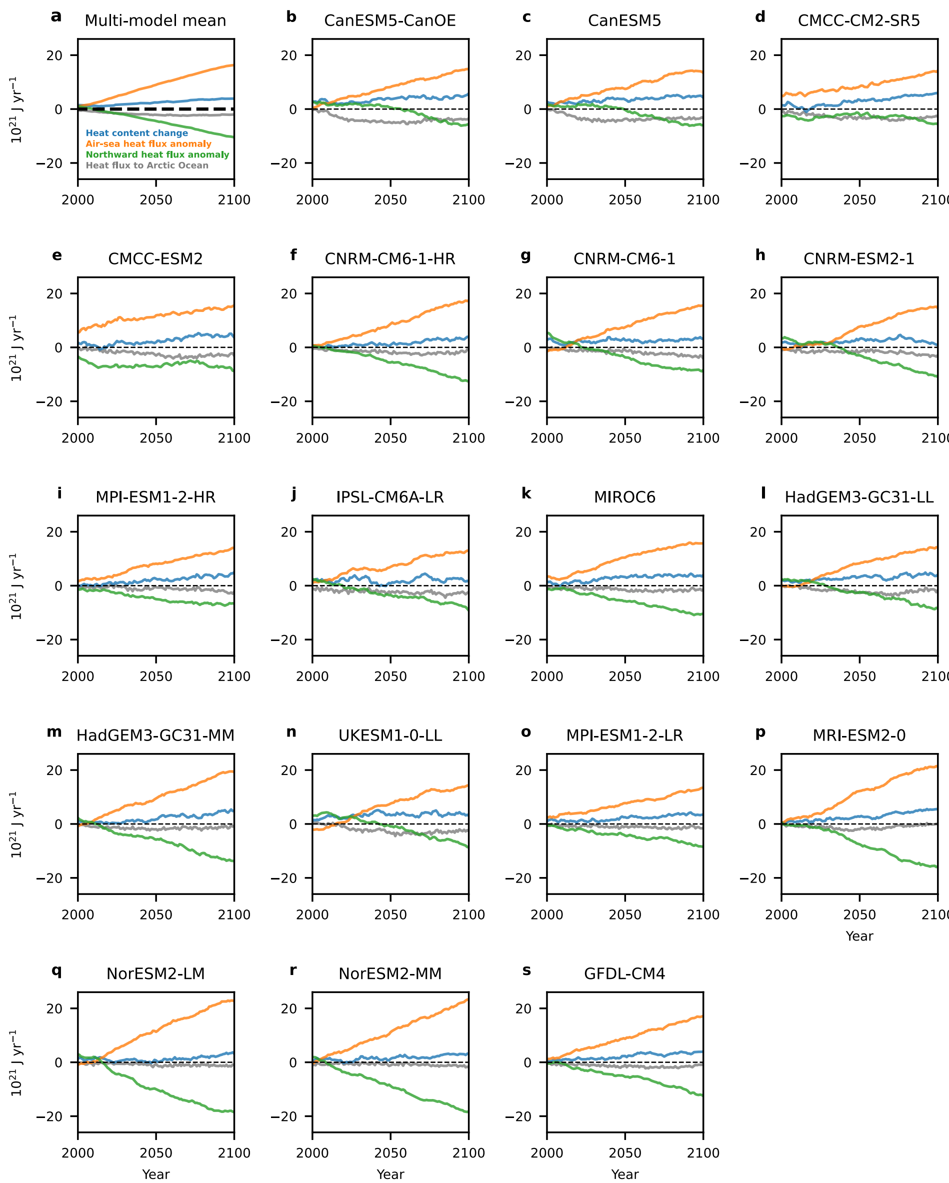

Supplementary Figure 10. Future North Atlantic heat budget north of 26.5°N from 2000 to 2100. Time series smoothed with a 10-year running mean of the North Atlantic ocean heat content change north of 26.5°N (blue), the anomaly of the air-sea heat flux in the same region (orange), the anomaly of the northward heat flux at 26.5°N (green), and the residual representing the heat flux to the Arctic Ocean (grey) for the **A)** multi model mean across an ensemble of 18 climate models and **B)** – **S)** for each model individually. The missing 6 climate models did not provide the northward heat transport and are therefore not shown here.

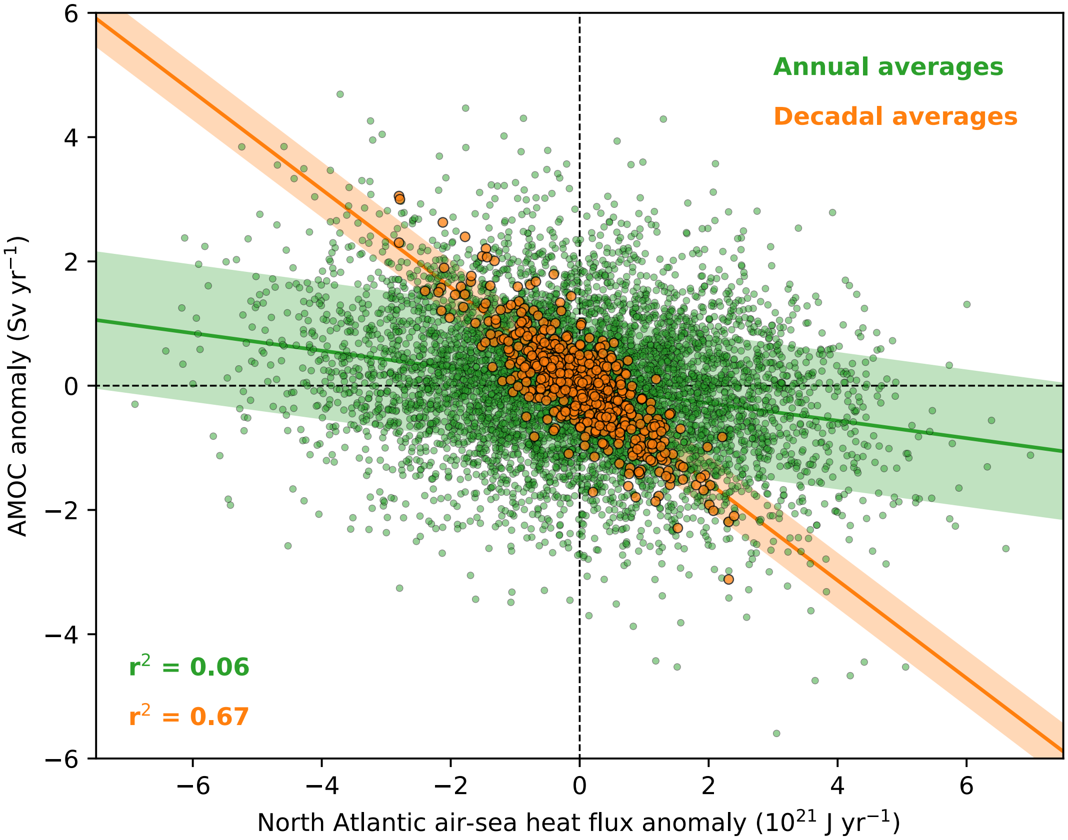

Supplementary Figure 11. AMOC anomalies at 26.5°N vs air-sea heat flux anomalies north of 26.5°N across climate models from CMIP6 at various timescales over the pre-industrial control simulation. The AMOC anomalies are calculated at 26.5°N for 24 climate models individually with respect to a linear trend over the time period in the pre-industrial AMOC simulations of each model that corresponds to the time period in the historical simulations. The North Atlantic air-sea flux anomalies north of 26.5°N are calculated with respect to linear trend over the time period in the pre-industrial AMOC simulations of each model that corresponds to the time period in the historical simulations. Blue dots indicate averages of the respective anomalies from 1850 to 2100. Orange dots indicate decadal averages of the anomalies from the 1850s to the 2090s. Green dots show annual averaged anomalies from 1850 to 2100. Positive heat flux anomalies indicate an increased heat flux from the atmosphere into the ocean.

123. Ziehn, T. *et al.* The Australian Earth System Model: ACCESS-ESM1.5. *J. South. Hemisph. Earth Syst. Sci.* **70**, 193–214 (2020).

124. Swart, N. C. *et al.* The Canadian Earth System Model version 5 (CanESM5.0.3). *Geosci. Model Dev.* **12**, 4823–4873 (2019).

125. Christian, J. R. *et al.* Ocean biogeochemistry in the Canadian Earth System Model version 5.0.3: CanESM5 and CanESM5-CanOE. *Geosci. Model Dev.* **15**, 4393–4424 (2022).

126. Danabasoglu, G. *et al.* The Community Earth System Model Version 2 (CESM2). *J. Adv. Model. Earth Syst.* **12**, (2020).

127. Cherchi, A. *et al.* Global Mean Climate and Main Patterns of Variability in the CMCC-CM2 Coupled Model. *J. Adv. Model. Earth Syst.* **11**, 185–209 (2019).

128. Lovato, T. *et al.* CMIP6 Simulations With the CMCC Earth System Model (CMCC-ESM2). *J. Adv. Model. Earth Syst.* **14**, e2021MS002814 (2022).

129. Voldoire, A. *et al.* Evaluation of CMIP6 DECK Experiments With CNRM-CM6-1. *J. Adv. Model. Earth Syst.* **11**, 2177–2213 (2019).

130. Séférian, R. *et al.* Evaluation of CNRM Earth System Model, CNRM-ESM2-1: Role of Earth System Processes in Present-Day and Future Climate. *J. Adv. Model. Earth Syst.* **11**, 4182–4227 (2019).

131. Held, I. M. *et al.* Structure and Performance of GFDL's CM4.0 Climate Model. *J. Adv. Model. Earth Syst.* **11**, 3691–3727 (2019).

132. Dunne, J. P. *et al.* The GFDL Earth System Model Version 4.1 (GFDL-ESM 4.1): Overall

Coupled Model Description and Simulation Characteristics. *J. Adv. Model. Earth Syst.* **12**, (2020).

133. Kelley, M. *et al.* GISS-E2.1: Configurations and Climatology. *J. Adv. Model. Earth Syst.* **12**, e2019MS002025 (2020).

134. Andrews, M. B. *et al.* Historical Simulations With HadGEM3-GC3.1 for CMIP6. *J. Adv. Model. Earth Syst.* **12**, e2019MS001995 (2020).

135. Sellar, A. A. *et al.* Implementation of U.K. Earth System Models for CMIP6. *J. Adv. Model. Earth Syst.* **12**, e2019MS001946 (2020).

136. Boucher, O. *et al.* Presentation and Evaluation of the IPSL-CM6A-LR Climate Model. *J. Adv. Model. Earth Syst.* **12**, e2019MS002010 (2020).

137. Tatebe, H. *et al.* Description and basic evaluation of simulated mean state, internal variability, and climate sensitivity in MIROC6. *Geosci. Model Dev.* **12**, 2727–2765 (2019).

138. Mauritsen, T. *et al.* Developments in the MPI-M Earth System Model version 1.2 (MPI-ESM1.2) and Its Response to Increasing CO_2. *J. Adv. Model. Earth Syst.* **11**, 998–1038 (2019).

139. Gutjahr, O. *et al.* Max Planck Institute Earth System Model (MPI-ESM1.2) for the High-Resolution Model Intercomparison Project (HighResMIP). *Geosci. Model Dev.* **12**, 3241–3281 (2019).

140. Yukimoto, S. *et al.* The Meteorological Research Institute Earth System Model Version 2.0, MRI-ESM2.0: Description and Basic Evaluation of the Physical Component. *J. Meteorol. Soc. Japan. Ser. II* **97**, 931–965 (2019).

141. Seland, Ø. *et al.* Overview of the Norwegian Earth System Model (NorESM2) and key climate response of CMIP6 DECK, historical, and scenario simulations. *Geosci. Model Dev.* **13**, 6165–6200 (2020).

142. Tjiputra, J. F. *et al.* Ocean biogeochemistry in the Norwegian Earth System Model version 2 (NorESM2). *Geosci. Model Dev.* **13**, 2393–2431 (2020).

143. Bi, D. *et al.* The ACCESS coupled model: description, control climate and evaluation. *Aust. Meteorol. Oceanogr. J.* **63**, 41–64 (2013).

144. Collier, M., Rotstayn, L., Kim, K.-Y., Hirst, A. & Jeffrey, S. Ocean circulation response to anthropogenic aerosol and greenhouse gas forcing in the CSIRO-Mk3.6 climate model. *Aust. Meteorol. Oceanogr. J.* **63**, 27–39 (2013).

145. Bao, Q. *et al.* The Flexible Global Ocean-Atmosphere-Land system model, Spectral Version 2: FGOALS-s2. *Adv. Atmos. Sci.* **30**, 561–576 (2013).

146. Watanabe, M. *et al.* Improved Climate Simulation by MIROC5: Mean States, Variability, and Climate Sensitivity. *J. Clim.* **23**, 6312–6335 (2010).

147. Yukimoto, S. *et al.* A New Global Climate Model of the Meteorological Research Institute: MRI-CGCM3 - Model Description and Basic Performance. *J. Meteorol. Soc. Japan. Ser. II* **90A**, 23–64 (2012).

148. Bentsen, M. *et al.* The Norwegian Earth System Model, NorESM1-M – Part 1: Description and basic evaluation of the physical climate. *Geosci. Model Dev.* **6**, 687–720 (2013).

149. Iversen, T. *et al.* The Norwegian Earth System Model, NorESM1-M – Part 2: Climate response and scenario projections. *Geosci. Model Dev.* **6**, 389–415 (2013).